Science and Technology Indonesia
e-ISSN:2580-4391 p-ISSN:2580-4405
Vol. 11, No. 2, April 2026

Research Paper

Evaluation of Photocatalytic and Catalytic Activity of Biochar/Nickel for Laboratory Wastewater Treatment

Is Fatimah[1,2*], Solekah[1,2], Nunung Nurlaela[1,2], Zeeshan Ahmad[1,2], Indah Tri Rizky[1,2], Azlan Kamari[3], Suresh Sagadevan[4], Ruey-an Doong[5]

[1]*Department of Chemistry, Faculty of Mathematics and Natural Sciences, Universitas Islam Indonesia, Kampus Terpadu UII, Sleman, Yogyakarta, 55584, Indonesia*
[2]*Nanotechnology and Sustainable Chemistry Research Centre, Universitas Islam Indonesia, Laboratorium Kimia, Kampus Terpadu UII, Sleman, Yogyakarta 55584, Indonesia*
[3]*Department of Chemistry, Faculty of Science and Mathematics, Universiti Pendidikan Sultan Idris, Perak, 35900, Malaysia*
[4]*Nanotechnology & Catalysis Research Centre, University of Malaya, Kuala Lumpur, 50603, Malaysia*
[5]*Department of Biomedical Engineering and Environmental Sciences, National Tsing Hua University, Hsinchu, 30013, Taiwan*
*__Corresponding author__: isfatimah@uii.ac.id

Abstract
In this investigation, an exploration on the use of low-cost effective methods for laboratory wastewater treatment using magnetic biochar has been conducted. Magnetic biochar derived from orange peel waste loaded with nickel nanoparticles (Biochar/Ni) was prepared by pyrolysis procedure of orange peel waste with nickel chloride as nickel precursor at 600 °C for 2 h. X-ray diffraction (XRD), scanning electron microscopy-energy dispersive x-ray (SEM-EDX), Raman spectroscopy, and vibrating sample magnetometer (VSM) were employed for identify the feature of Biochar/Ni. Photocatalytic, photocatalytic oxidation, and microwave-assisted catalytic peroxidation were the treatment procedures employed to evaluate the activity of Biochar/Ni. The results showed the dispersed nickel nanoparticles in the composite are photocatalytic system to produce radicals for decolorizing laboratory wastewater as proven by accelerated oxidation by the addition of H_2O_2 and $S_2O_8^{2-}$ as oxidants, and inhibition by the addition of radicals and superoxide radical scavengers. In addition, microwave-irradiation intensified catalytic peroxidation with shorter time and higher decolorization efficiency. The greenness evaluation of the process using AGREE software addressed the microwave-assisted catalytic peroxidation as the most efficient procedure utilizing Biochar/Ni for being developed and implemented to organic contaminated wastewater.

Keywords
Biochar, Magnetic, Microwave-Assisted Reaction, Nickel-Biochar, Photocatalysis

Received: 15 December 2025, Accepted: 22 February 2026
https://doi.org/10.26554/sti.2026.11.2.579-595

1. INTRODUCTION

Environmental safety is an irrefutable problem which is challenging to be taken up as environmental quality will be linked to many aspects for development. Within the scheme, monitoring on water quality and organic-contaminated wastewater treatment are to be concerned. These include of organic compounds such dyestuffs, polycyclic aromatic hydrocarbons, perfluorinated compounds, dioxins, dioxanes, and other emerging pollutants pesticide, that are mainly organic compound with high molecular weight (Methneni et al., 2021; Fouda et al., 2025). According to the Stockholm Convention, a variety of compounds which the physical properties such as hydrophobicity, potential bioaccumulation, and toxicity constitute their great persistence in the environment, and known as persistence organic pollutants (PoPs) (Bekru et al., 2022).

Not only from industrial activities, but laboratory wastewater also containing highly persistent organic chemicals need to be monitored. So far, in education laboratories, including in the university, wastewater was treated by third parties. Various processes including oxidation, biological treatments and incineration were attempted. In addition, advanced oxidation processes (AOPs) are well-known procedure to remove organic compounds-contaminated water (Fatimah et al., 2022a).

In fact, some functional materials are produced from material research activities, and by using the model compounds there are success story of pollutant removal via adsorption, catalytic oxidation, and some intensified oxidation (Thiruvenkatachari et al., 2008; Li et al., 2023). However, applicability of prepared functional materials for the removal of PoPs from laboratory wastewater is not recognized yet. With the vision of zero-waste and maintaining sustainable and green campus, examination of functional material for laboratory wastewater treatment is a good starting point.

Recently, biochar-based functional materials have been explored for various applications such as adsorption and catalysis. With a simple procedure of preparation and abundant

resources of carbon-rich solids that could be derived from many biological sources including agricultural waste, 'biochar is notified as low-cost materials (Rahayu et al., 2020; Lesbani et al., 2021a). In addition, the functionalization biochar with designing magnetic properties is one strategy to improve applicability by simple external magnetism (Fitri et al., 2024; Palapa et al., 2024). From many research works, the magnetism support reusability and easy recyclability (Lesbani et al., 2021b). Besides iron oxide-based magnetic biochar, the dispersion of nickel nanoparticles into biochar exhibited magnetism with high chemical stability. Previous work reported the capability of Ni/biochar from palm leave waste to degrade methyl violet in photocatalytic and photocatalytic oxidation treatment (Fatimah et al., 2024). Biochar is a carbon-rich solid that could be obtained by heating biomass in an oxygen-depleted environment. Within these categories, food and agricultural waste are highly potential raw materials.

Orange peel is abundantly obtained as food and agricultural waste and underutilized (Wanapat et al., 2024; Vilas-Boas et al., 2025). Moreover, the examination of nickel/biochar for intensive laboratory wastewater treatment is interesting and important to be explored. Nickel nanoparticles showed surface plasmon resonance photo-activated radicals' formation, and in other mechanism, it is capable to activate peroxidation (Palapa et al., 2024). Based on previous reports highlighting the potentiality of nickel nanoparticles in AOPs, comparison of photocatalytic process with intensified catalytic peroxidation is studied in this work. Among some intensified AOPs such as ultrasound-assisted process, microwave (MW)-assisted oxidation, and photon/UV-assisted oxidation, MW-assisted reaction is the leading procedure due to shorter reaction times and improved efficiency.

The aims of this work are to study physicochemical characteristics of nickel-loaded biochar derived from orange peel (furthermore called as Biochar/Ni) and evaluate its effectiveness in AOPs procedures for laboratory wastewater treatment. Photocatalytic treatment, photocatalytic oxidation, and MW-assisted catalytic peroxidation of laboratory waste were compared based on kinetics and greenness evaluations.

2. EXPERIMENTAL SECTION

2.1 Material

Orange peel waste was collected from traditional market in Sleman District, Yogyakarta Special Region of Indonesia. Other chemicals consist of nickel chloride hexahydrate, isopropanol (IPA), benzoquinone (BQ), H_2O_2, and ammonium peroxodisulfate were obtained from Merck (Darmstadt, Germany). All chemicals were used as received without any purification. Laboratory waste samples were collected from 4 (four) laboratory of Universitas Islam Indonesia.

2.2 Methods

2.2.1 Preparation of Biochar/Ni

Biochar/Ni was prepared by one-pot pyrolysis procedure. Initially, orange peels were chopped and dried in an oven followed by mixing with the precursor solutions of nickel chloride to get nickel percentage of 10 %wt. The mixture was stirred followed by water evaporation. The dry solid was pyrolyzed at 600 °C for 2 h in a tubular pyrolysis reactor under N_2 stream. The final powder of Biochar/Ni was collected for physicochemical characterization and catalytic and photocatalytic activity examinations.

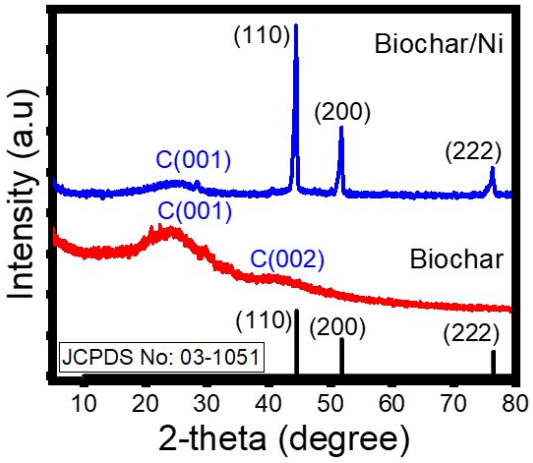

Figure 1. XRD Pattern of Biochar/Ni in Comparison with Biochar and JCPDS No: 03-1051

2.2.2 Characterization

Physicochemical characteristics of the prepared Biochar/Ni were analyzed using x-ray diffraction (XRD) analysis on Miniflex Rigaku (Japan), scanning electron microscope-energy dispersive x-ray fluorescence (SEM-EDX) JEM-JEOL (Japan), Raman spectroscopy (RAMAN), and vibration sample magnetometer (VSM)-BHV-5 (Japan). For XRD analysis, the Ni-filtered Cu Kα was used as radiation source and the measurement was recorded at 2θ ranging at 10-80°.

2.2.3 Photocatalytic and Photocatalytic Oxidation of Laboratory Wastewater

Photocatalytic oxidation of laboratory wastewater (LW) samples was performed in a batch photocatalytic reactor equipped with UV Lamp (Philips, 20Watt, 296 nm). About, 0.1 g of Biochar/Ni and 10^{-3} M of H_2O_2 were added into 250 mL LW sample, then the mixture was stirred for 15 min prior UV light exposure. The time before UV exposure was applied to gain adsorption equilibrium, and initial time of stirring was noted as -15 min of treatment. The color changes during treatment were identified as the occurring reaction, and the decolorization efficiency was determined by measuring the absorbance of the sample on by UV-Visible spectrometer (HITACHI U-2080) at each maxima wavelength. The decolorization efficiency was calculated based on the following Equation (1):

$$\text{Decolorization efficiency (\%)} = 100 \times \frac{[Abs_0] - [Abs_t]}{[Abs_0]} \quad (1)$$

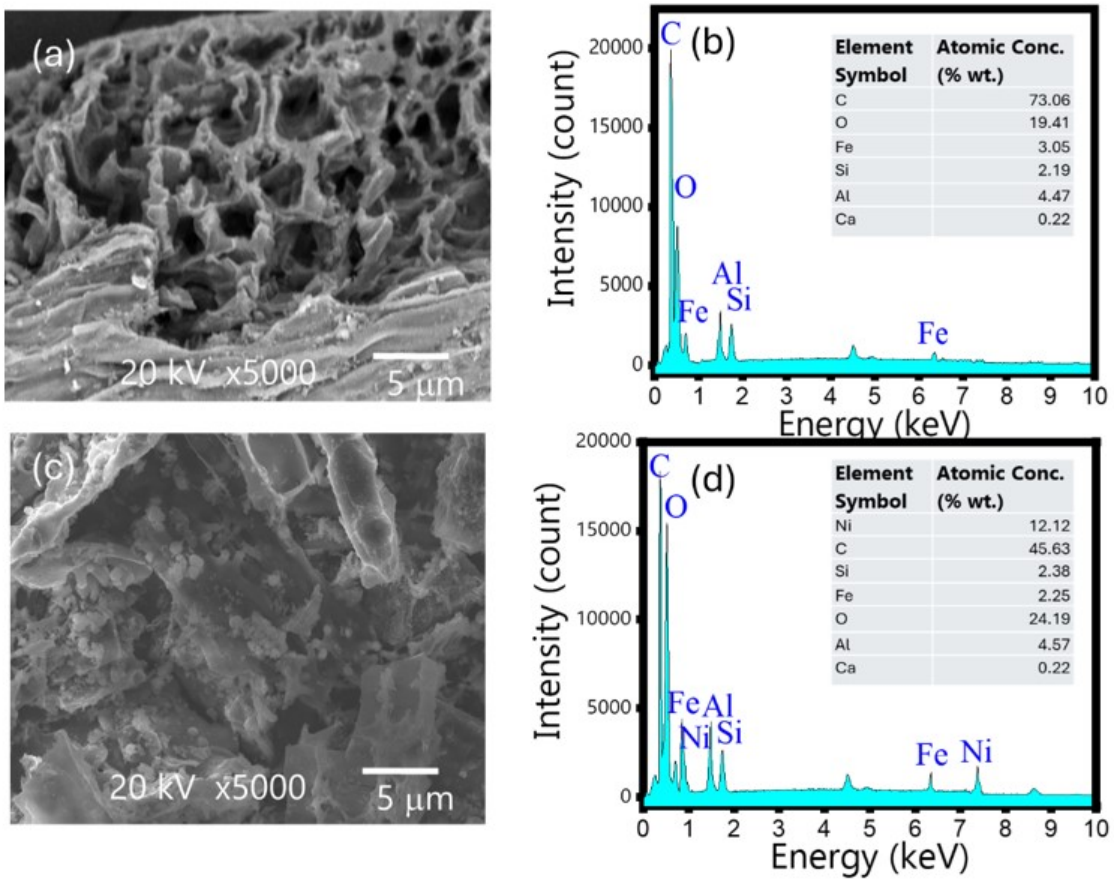

Figure 2. (a-b) SEM Image and EDX of Biochar, (c-d) SEM Image and EDX of Biochar/Ni

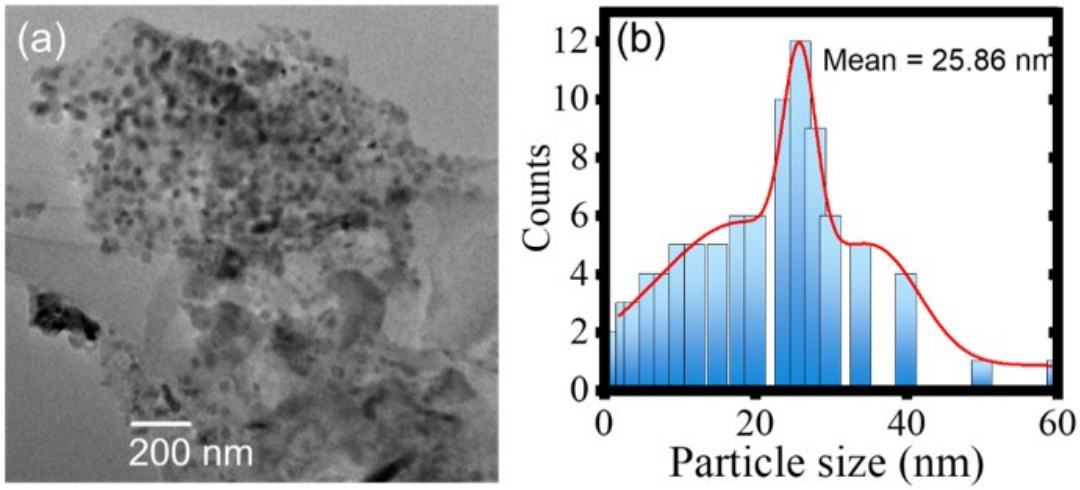

Figure 3. a) TEM Image and (b) Particle's Size Distribution of Biochar/Ni

with Abs_0 and Abs_t are the initial absorbance and absorbance at time of t of the sample.

Similar procedure was applied for photocatalytic treatment, but the mixture was without H_2O_2 or ammonium peroxodisulfate as oxidant. of powder followed by the addition of 5×10^{-3} M of H_2O_2.

Besides the decolorization efficiency analysis, chemical oxygen demand (COD) analysis was also performed by using re-

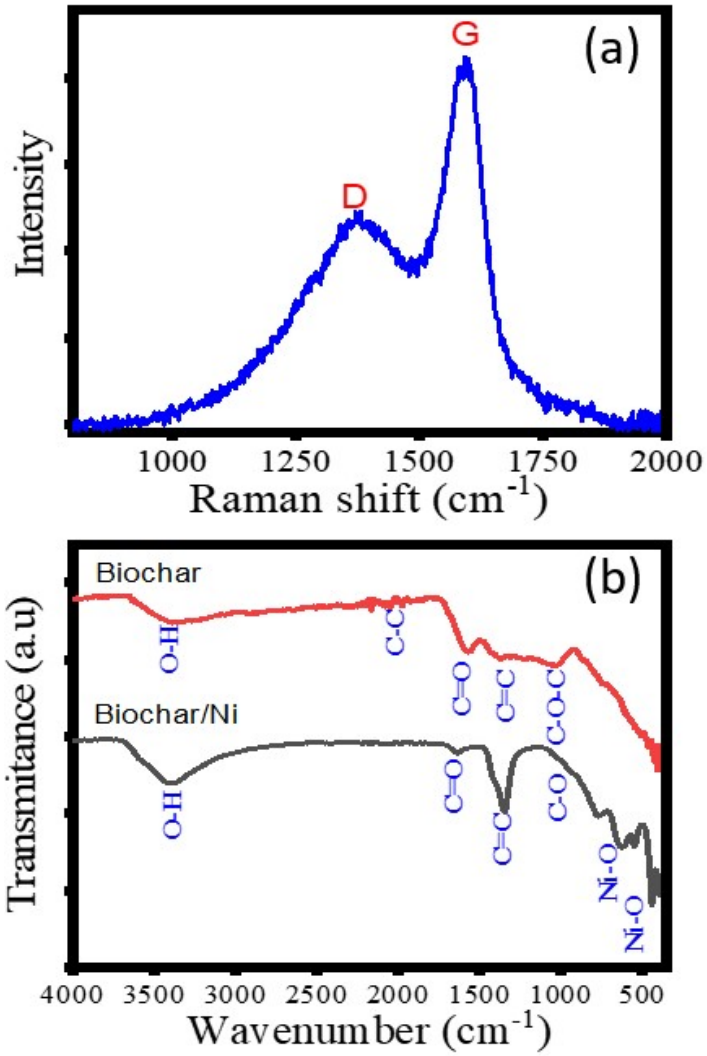

Figure 4. (a) Raman Spectrum of Biochar/Ni, (b) FTIR Spectrum of Biochar/Ni in Comparison to Biochar

Table 1. Calculated Crystallite Size Based on XRD Analysis

2θ	Reflection index	FWHM	Crystallite size (nm)
44.37	110	0.378	25.21
51.71	200	0.414	23.71
76.22	222	0.408	27.51
Crystallite size mean			25.47

flux method followed by spectrophotometric analysis. The procedure of analysis includes refluxing water samples with potassium dichromate and digested reagent followed by spectrophotometric measurement (typically at 440 nm or 600–620 nm) for calculating the remaining dichromate. Potassium dihydrogen phosphate was employed for determining callibration standard.

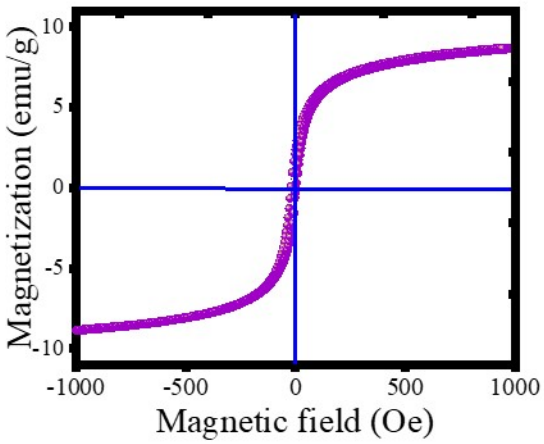

Figure 5. Magnetization VSM Plot of Biochar/Ni

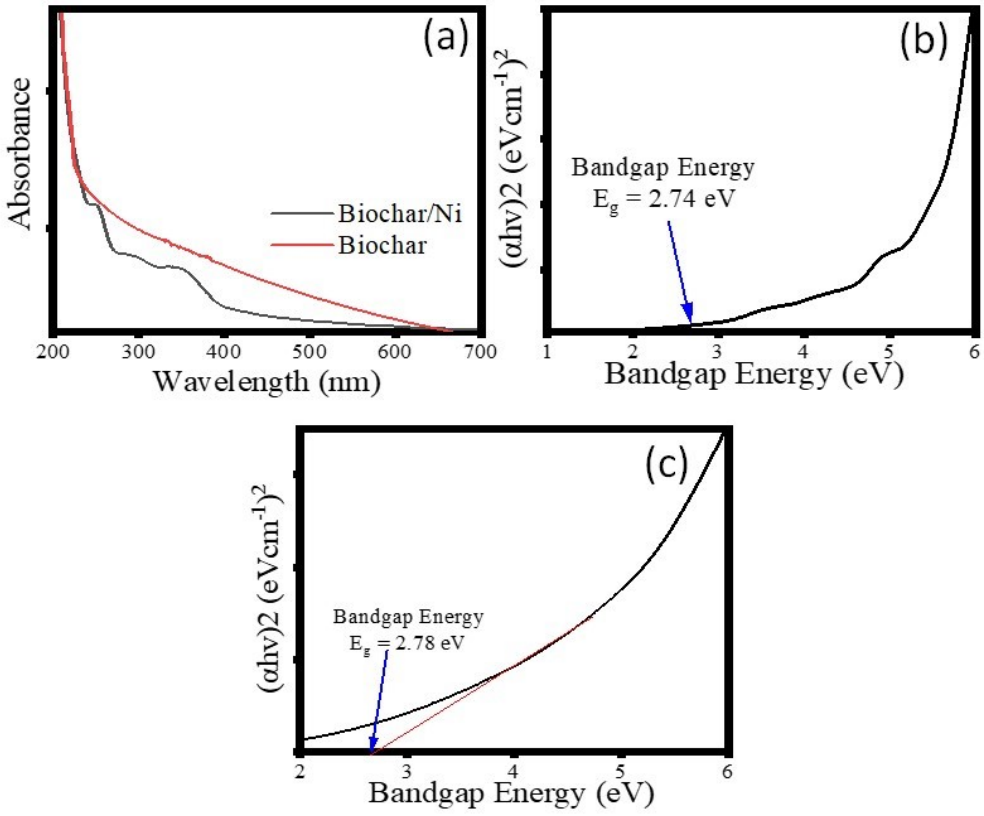

Figure 6. (a) UV-DRS Spectra of Biochar and Biochar/Ni, (b-c) Tauc's Plot of Biochar/Ni and Biochar, Respectively

Table 2. Calculated Textural Parameters from Adsorption-Desorption Isotherm Analysis

Parameter	Biochar	Biochar/Ni
BET specific surface area (m^2/g)	23.11	59.71
Pore radius (nm)	9.12	7.20
Pore volume (cm^3/g)	4.31×10^{-3}	1.11×10^{-2}

2.2.4 Microwave-Assisted Catalytic Peroxidation of Laboratory Wastewater

MW-assisted catalytic peroxidation of LW sample was conducted on a batch reactor which can accommodate a 1-L reflux system equipped with cooling water equipped with MW irradiation source (Philips, 2.54 GHz) operated in a continuous mode. Each reaction was operated within an interval of 10 min at a power of 200 W and a maximum temperature of 40 °C. The samples were taken consecutively for analysis using UV-Visible spectrophotometric analysis and COD measurement similar to the photocatalytic and photocatalytic oxidation treatment.

3. RESULT AND DISCUSSIONS

3.1 Biochar/Ni Characterization

The characterization using XRD analysis gives the reflections depicted in Figure 1 demonstrating that BC shows a broad peak at 2θ ranging at 20-28° with maximum point at 24° together with less intensive broad peak at 41.8°. The peaks are associated with the crystal plane index of C(002) and C(001) which are related to the parallel and azimuthal orientation of the aromatic and carbonised structure, respectively. The high symmetry of the C(002) peak indicates the absence of γ-bands linked to amorphous and aliphatic structures, while the broad peak assigned to C(100) reflect the size of the aromatic lamina or graphene layers in the biochar (Yeboah et al., 2020; Yan et al., 2021; Fatimah et al., 2022c). The intensities of these peaks are reduced in BC/Ni along with the intensive peaks positioned at 2θ of 44.37°, 51.71°, and 76.22° that are corresponding to the presence of Ni nanoparticles (NiNPs) as confirmed by the appropriateness to the JCPDS No 03-1051 (Jahani et al., 2023; Rehman et al., 2023). The lower intensity of the C(002) and C(001) reflections from carbonaceous structure in Biochar/Ni is due to high crystallinity of dispersed

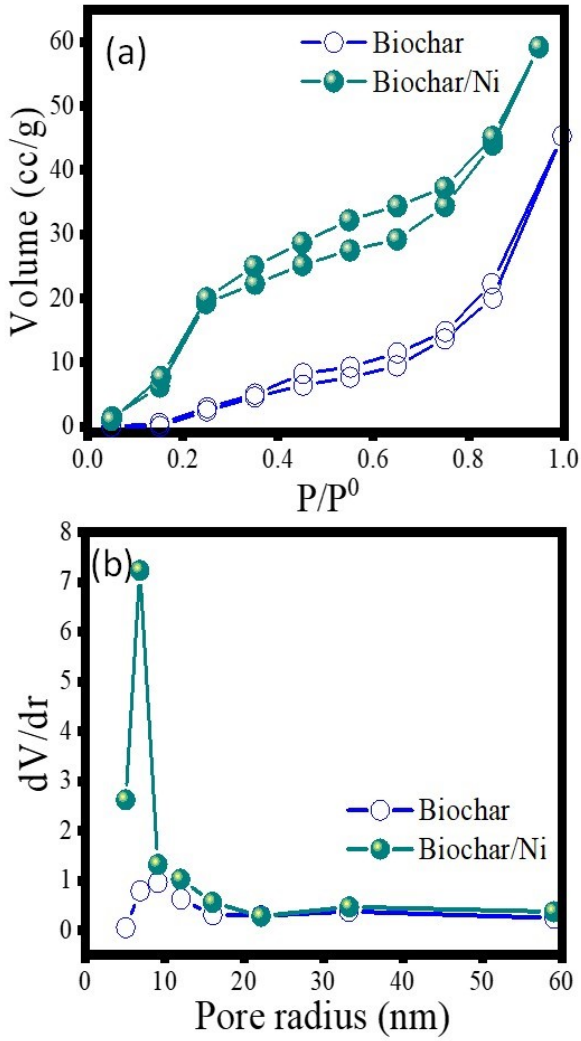

Figure 7. (a) Adsorption-Desorption Isotherm, (b) Pore Size Distribution of Biochar/Ni in Comparison With Biochar

nickel nanoparticles. This suggests the homogeneous dispersion of nickel nanoparticles in high crystallinity in biochar matrix. Similar phenomena were also reported in the dispersion of Ag@Biochar and NiO@biochar (Eltaweil et al., 2022; Phyu et al., 2023). Using Scherer equation defined elsewhere, the calculation of crystallite size as presented in Table 1 gave the value of Based on (110) peak of nickel, the calculated crystallite size is 25.47 nm.

The confirmation is reflected by SEM-EDX analysis results provided in Figure 2. Surface profile of Biochar composed of porosity which similar to other reported characteristic biochar surfaces (Tomczyk et al., 2020; Lesbani et al., 2021a; Fatimah et al., 2022b). By the modification with nickel nanoparticles, some distributed spheric particles appeared. The elemental analysis shows that carbon and oxygen are the main constituents of Biochar and Biochar/Ni. Additionally, the presence of Fe, Al, and Si is identified in both materials caused by the nature of the raw material. The Ni content in Biochar/Ni is detected as around 12 %wt., which is nearly with the set-up content of 10 %wt., and it is absence from Biochar.

Detail on morphology of the dispersed nickel nanoparticles in Biochar/Ni was examined using TEM analysis, and the image is presented in Figure 3. The well-dispersed irregular spherical particles with an average diameter of around 10–60 nm are expressed by the image. By the calculation on particle's size distribution, the mean diameter of the particles is 25.86 nm. This value is in line with the result from the calculation on crystallite size using XRD measurement. Both the identified morphology and size range are similar to the multicomponent Co-Ni/Biochar reported using poplar wood as raw material (Bao et al., 2024) and Ni/Biochar prepared using wood chips (Zulqarnain et al., 2025).

Table 3. Characteristics of LW Samples

Laboratory Waste	Laboratory activities	COD (mg/L)
LW1	Thesis and undergraduate's research on the development of materials for dye and organic contaminated water	970
LW2	Laboratory work of undergraduate students	833
LW3	Undergraduate research on physical, inorganic, and organic chemistry laboratory works including organic synthesis, sensor development and materials for water treatment treatment	2773
LW4	Thesis and undergraduate research on environmental remediation including biological, physical and chemical simulation treatments for industrial wastewater water	807

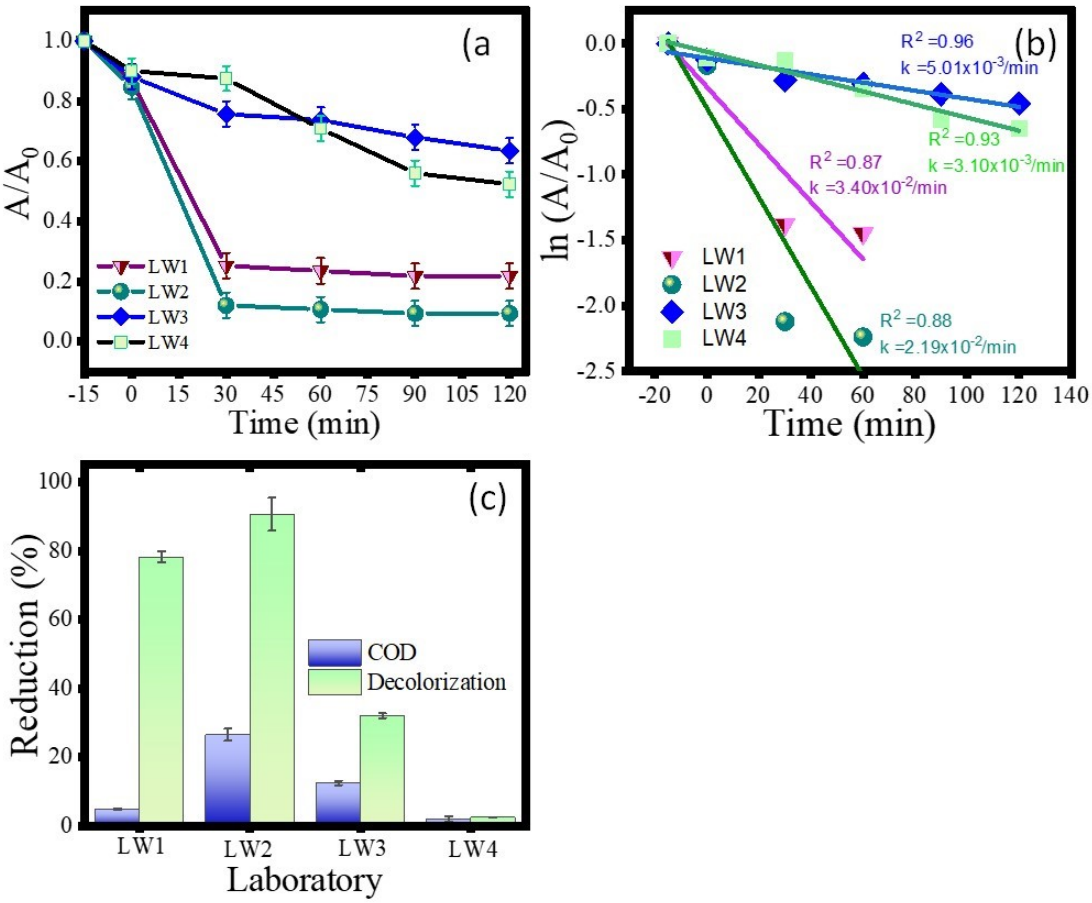

Figure 8. (a) Kinetics of LW Decolorization by Photocatalytic Oxidation Treatment Using Biochar/Ni, (b) Pseudo-First Order Plots of Decolorization, (c) COD and Decolorization Reduction [Condition: Photocatalyst Dose = 0.1 g/250 mL, H_2O_2 = 10^{-3} M, pH = 7, Light: UV 296 nm, 20 Watt]

Raman spectroscopy was employed to investigate the graphitization state in Biochar/Ni, and the spectrum is shown in Figure C. From Figure 4a, it is seen that the Biochar/Ni demonstrates two characteristic peaks observed at ~1381 and ~1599 cm^{-1} that are corresponding to the D and G peaks for carbon materials (Bhakta et al., 2025). The D peak is associated to sp^3 hybridization of carbon atoms, disordered vibration of carbon atoms, and defects of carbon atoms, while the G peak is at-

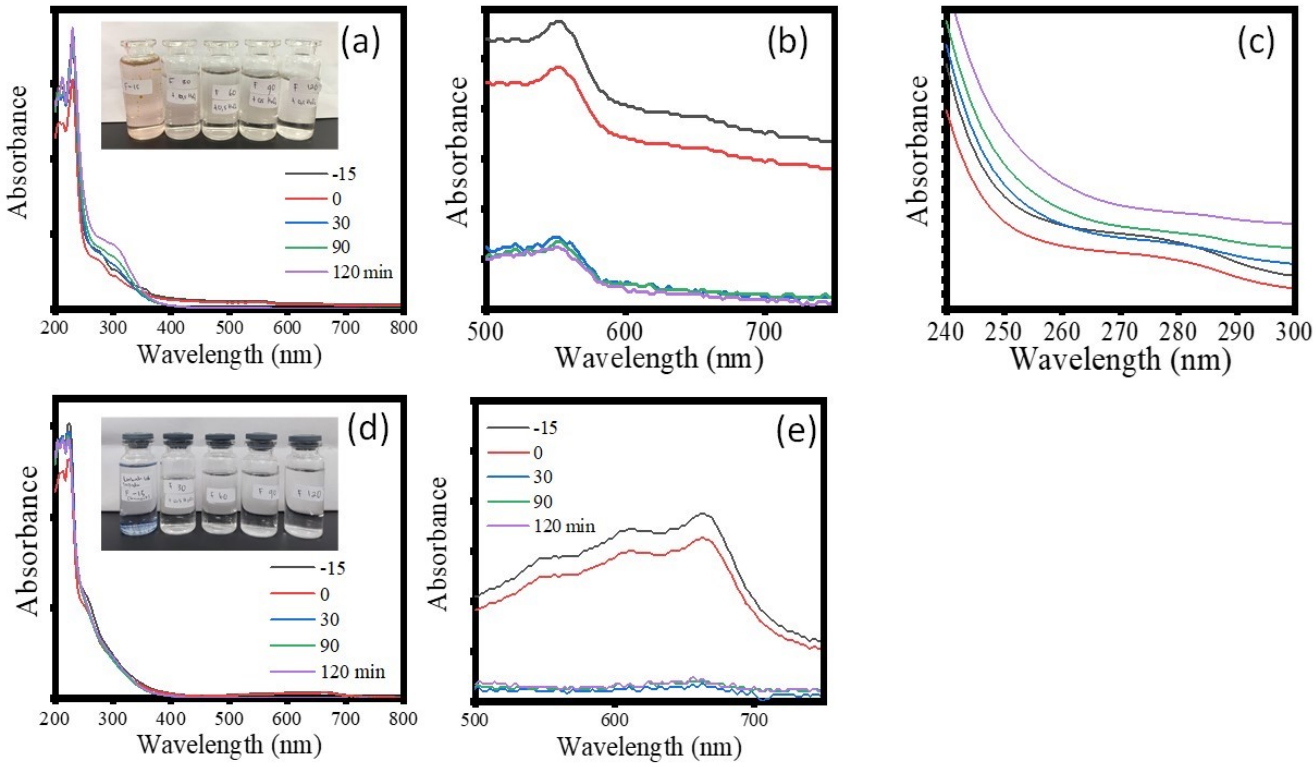

Figure 9. Spectral Change of (a-c) LW1, (d-e) LW2 by Photocatalytic Oxidation Treatment Using Biochar/N

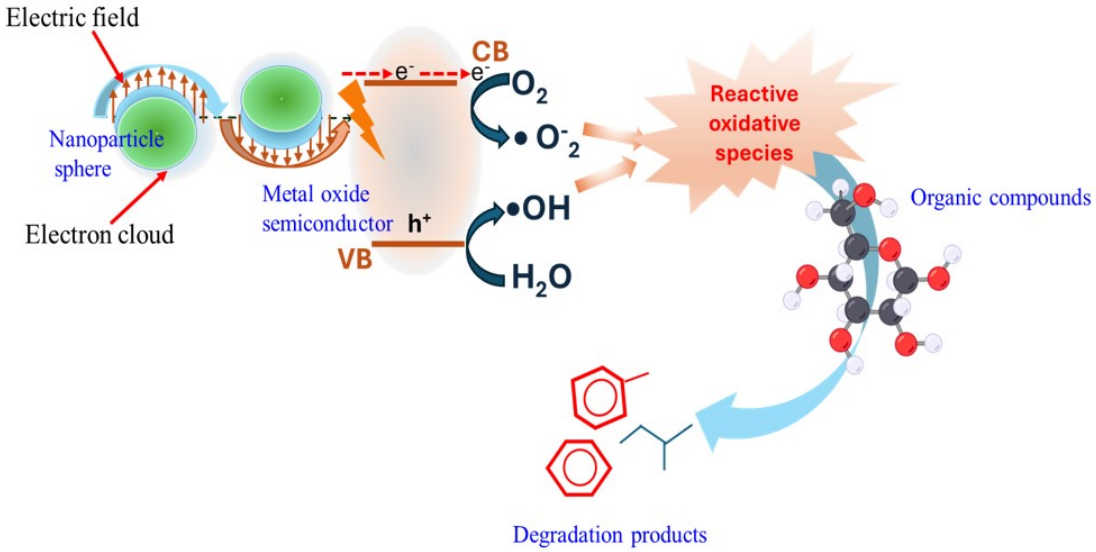

Figure 10. Surface Plasmon Resonance Mediated Photocatalytic Degradation of Organic Compounds (Talebi et al., 2021)

tributed to in-plane telescopic vibration of sp^2 hybridization of carbon atoms. From many investigations, the ratios between D and G peaks (I_d/I_g), which reflect the acuteness of defects and disorders as the low I_D/I_G value implies an orderly graphite structure with a high graphitization degree in the carbon structure. The calculated I_d/I_g is 0.56, represents that low structural defects is in Biochar/Ni structure, compared to was reported by $ZnCl_2$-supported biochar (Moreno et al., 2022), and nickel-supported H_3PO_4-activated biochar (1.23) (Hu et al., 2024). It suggests that there is insignificant defect which nickel pre-

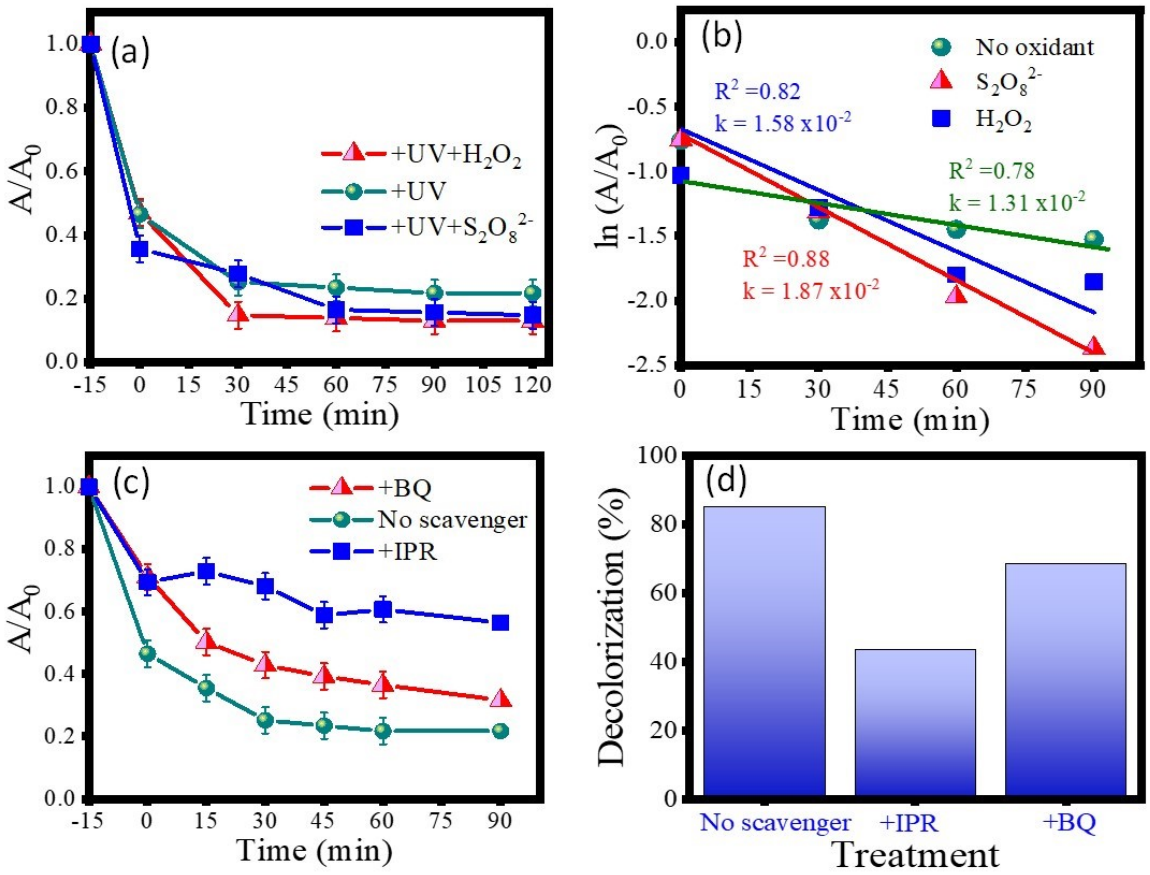

Figure 11. a) Kinetics Plots of Photocatalytic Oxidation in Comparison to Photocatalytic Treatment (+UV), b) Pseudo-First Order Kinetics Plot of Photocatalytic Oxidation and Photocatalytic Treatment, (c-d). Kinetics Plots and Decolorization Efficiency in the Addition of Radical's Scavenger, Respectively. [Condition: Photocatalyst Dose = 0.1 g/250 mL, H_2O_2 = 10^{-3} M, pH = 7, Light: UV 296 nm, 20 Watt]. (Talebi et al., 2021)

cursor catalyzes the nanostructure formation during carbon graphitization as reported by the use of iron (Hunter and Ram, 2022) and Ni promotes sp^3 to sp^2 hybridization and intensified carbonate decomposition benefiting the regular structure and low degree of disorder (Hu et al., 2024).

The embedded Ni in Biochar/Ni is also confirmed by the compared FTIR spectra between Biochar and Biochar/Ni [Figure 4b]. Both Biochar and Biochar/Ni show the strong wide band at 3410 cm^{-1} as the identification of stretching vibrations of O–H from occurring converted cellulose, lignin, and hydroxyl groups of polysaccharides. Some weak peaks positioned at around 2900-2945 cm^{-1} are attributed to C-C stretching representing the $-CH_3$ and $-CH_2$ groups of aliphatic compounds. The absorption peak at around 1640 cm^{-1} implies the C = O stretching from occurrence of the ester groups. The representation of graphitic structure is confirmed by C = C absorption band observed at 1550 cm^{-1}. The glycosidic functional groups are identified by absorption at 1032 cm^{-1} which belong to ethers. The presence of Ni is indicated by Ni–O bonds fingerprint vibrations at 544 and 634 cm^{-1} (Moavi et al., 2021; Khan et al., 2022).

Vibrating Sample Magnetometer (VS) characterization was performed to investigate the magnetism of Biochar/Ni, and the data is depicted in Figure 4. VSM shows a Hysteresis loop suggesting a soft magnetic property with saturated magnetism of value of 8.64 emu/g. The value is lower compared to Ni-loaded biochar prepared using palm leaves with a value of 13.7 emu/g for pure magnetite and 9.67 emu/g in the composite, but higher compared to Ru-dithizone@biochar/Ni (4.72 emu/g) (Moradi and Hajjami, 2022). Shielding carbon effect in biochar support causes the lower magnetic field, as the nickel nanoparticles magnetism was reported as 45.71 emu/g.

Optical property of Biochar/Ni is investigated by measuring the absorption spectra and correlated Tauc's plots based on the UV-DRS spectroscopy. The absorption spectra of both Biochar and Biochar/Ni reflect that the materials absorb light within the UV and visible region, which Biochar/Ni shows a slightly higher absorbance compared to Biochar [Fig-

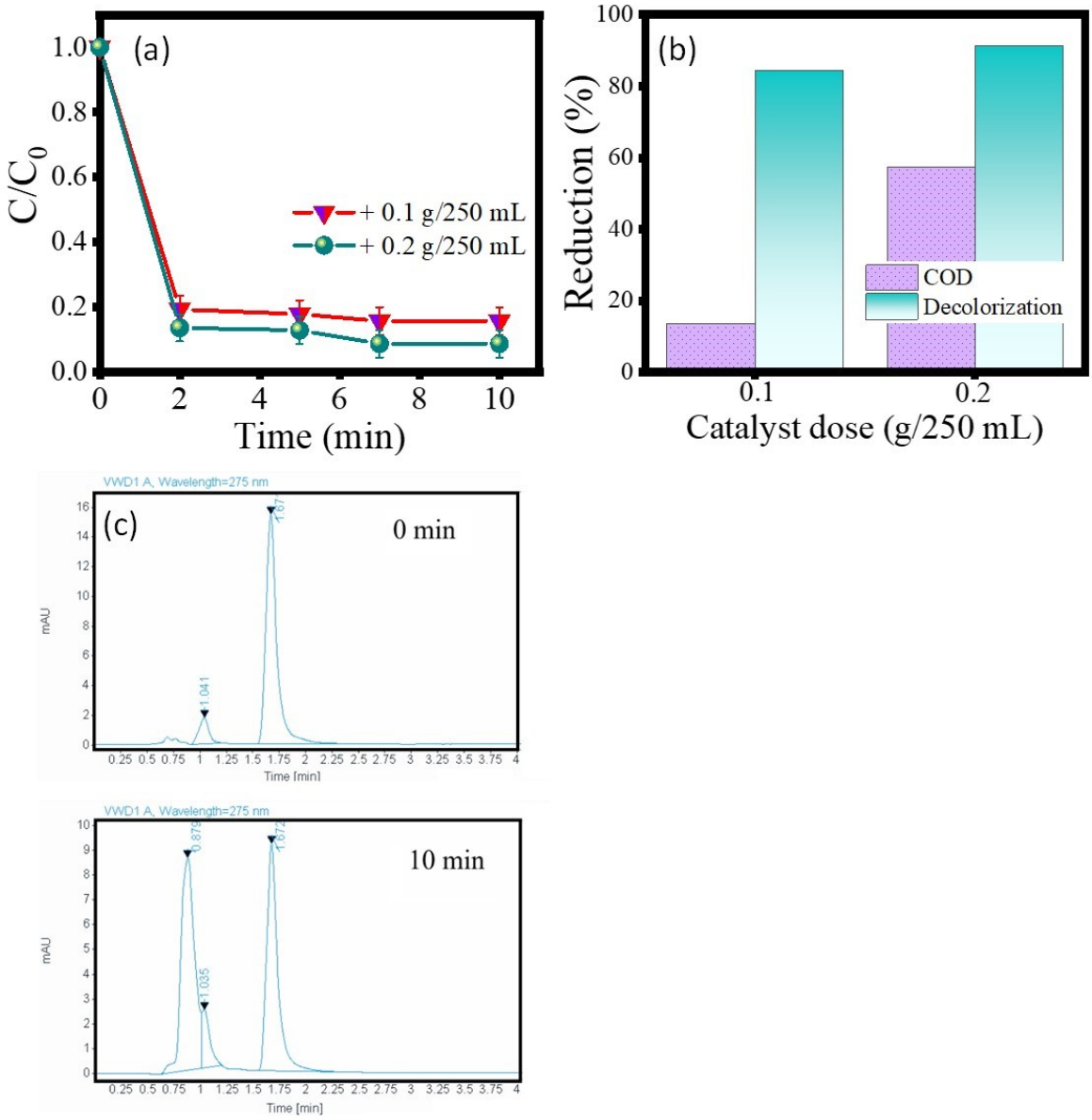

Figure 12. (a-b) Kinetics Plots, Decolorization and COD Reduction of MW-Assisted Catalytic Peroxidation, Respectively, c) HPLC Chromatograms of Initial LW and Treated LW for 10 Min

ure 6a]. The absorption patterns are similar to was reported by Biochar@ ZnO/Ce (Jahani et al., 2023). The band gap energy of the materials was measured based on following equation:

$$(\alpha h\nu)^2 = A(h\nu - E_g) \quad (2)$$

where α is the absorption coefficient (cm^{-1}), ν is the photon energy (eV), A is the constant of the equation, and Eg is the energy of the band gap energy. The Tauc's plots based on this equation gave the observed band gap energy of Biochar and Biochar/Ni are 2.78 eV and 2.74 eV, respectively [Figure 6b-6c]. The insignificant difference of the band gap energy between both materials is referred to that nickel nanoparticles are not semiconductor material, so the band gap energy is represented from some the metal oxide components in Biochar such as iron oxide.

As the nickel dispersion contributes to changing the biochar surface and magnetism, it generally influences the textural properties including specific surface area, pore distribution, and pore radius. Figure 7a presents the adsorption isotherm curves

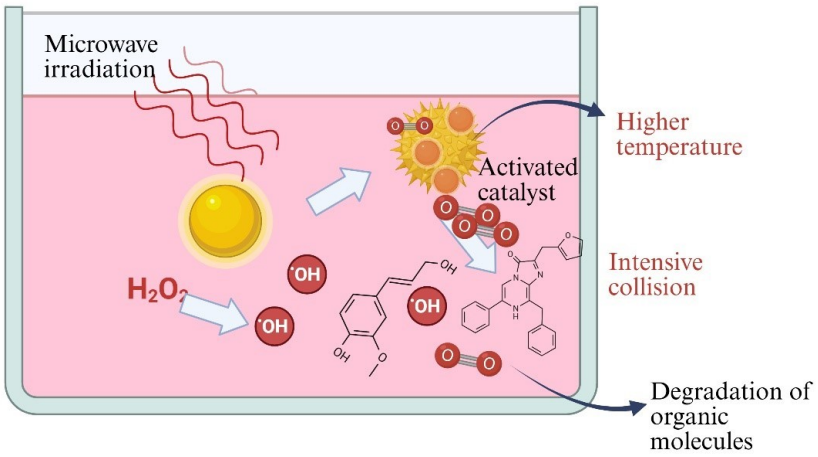

Figure 13. Mechanism of MW-Assisted Catalytic Peroxidation Reaction

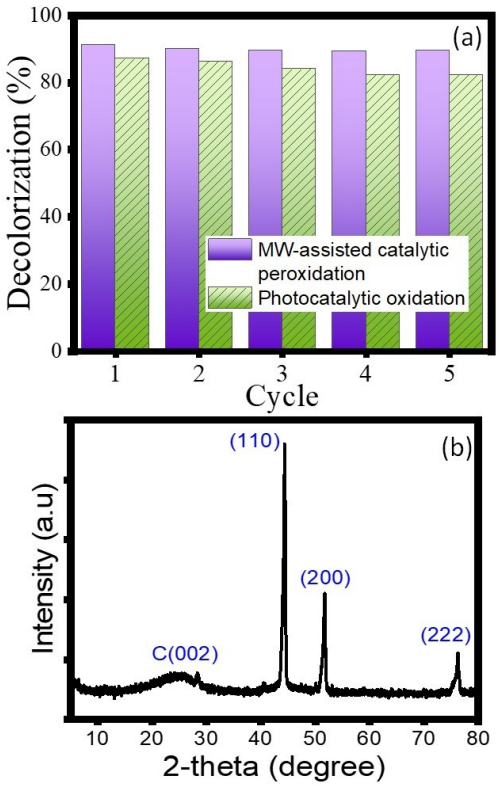

Figure 14. a) Reusability Test of Biochar/Ni in Photocatalytic Oxidation and MW-Assisted Catalytic Peroxidation

of Biochar and Biochar/Ni, and based on the isotherm data, the determined pore distributions of Biochar and Biochar/Ni are depicted in Figure 7b. The resumed parameters are listed in Table 2.

A considerable difference of the isotherm is expressed as Biochar isotherm behaves as type V referred to IUPC classification of isotherm, which represents non-porous material. Meanwhile, Biochar/Ni exhibited the type IV isotherms as a hysteresis loop is presented, and this indicates a wide mesopore distribution. These facts are associated with the increasing BET specific surface area of Biochar after nickel nanoparticles dispersion, from 23.11 m^2/g into 59.71 m^2/g. Consequently, by BJH desorption data, the calculated pore volumes are from 4.31×10^{-3} cm^3/g into 1.11×10^{-2} cm^3/g for Biochar and Biochar/Ni, respectively. The pore size distribution demonstrated that there is a significant intensity of the pores ranging at 5–10 nm. From the calculation, the mean pores radius of Biochar and Biochar/Ni are 9.12 nm and 7.20 nm, respectively. The isotherm pattern and calculated textural parameters are similar to the measured from biochar obtained from pea peels (El-Nemr et al., 2024), sugarcane (Barría et al., 2025), and lignin (Li et al., 2024).

3.2 Photocatalytic Activity of Biochar/Ni

The catalytic and photocatalytic effects of Biochar/Ni for different laboratory wastewater was examined using varied conditions. MW-assisted peroxidation towards LW1-LW4 samples. The samples were laboratory waste from different characteristics of laboratory activities, with the details provided in Table 3.

The photocatalytic activity of Biochar/Ni was examined on LW decolorization under photocatalytic oxidation treatment using a water-jacketed batch photoreactor equipped with UV lamp (20 Watt, Philips). The kinetics plots presented in Figure 8a were derived from measured absorbance at the maximum wavelength of each wastewater. All photocatalytic treatments reduced the colour of the LW samples as identified by reduced absorbance (A/A_0) along the increased time of treatment. As the absorbance represents color and not proportionally respect to the contaminant in the wastewater, the term decolorization is utilized. It is obtained that the decolorization of LW2 is

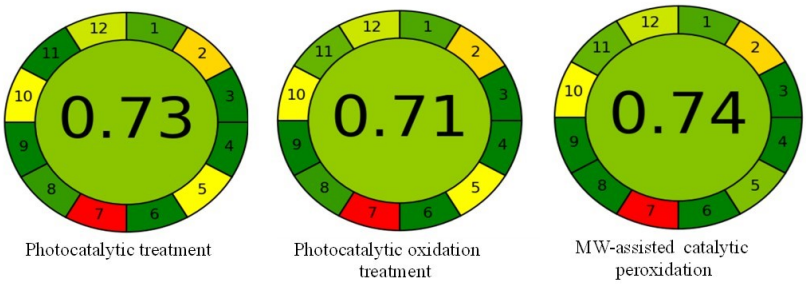

Figure 15. GREE Score and Corresponding Pie Charts of the Examined Process

in the highest value, and in detail the removal rate is in following order: LW2> LW1>LW4>LW3. Kinetics study on LW photocatalytic oxidation treatment was performed, and it is concluded that all decolorization obeys pseudo-first order kinetics referred to kinetics Equation (3):

$$\ln \frac{C_0}{C_t} = k_{app}t \tag{3}$$

with k_{app} is apparent kinetics constant and C_0 and C_t are initial concentration and the concentration at time of t, respectively. The fitness of kinetics data, correlation coefficients and calculated k_{app} are provided in Figure 8b. Referring to the kinetics plots of LW1 and LW2 decolorization showing an equilibrium condition achievable at 60 min, the pseudo-first order kinetics for both samples were applied until 60 min. In this case, the ratio absorbance was taken by the principle that absorbance is linearly correlated to concentration. The kinetics constants of the treatments are consistent with the decolorization efficiencies. Based on the COD measurement, the COD removal of each LW sample [Figure 8c] shows that the decolorization rate is not linearly correlated to the degree and concentration of contaminants as identified by COD value. LW4 has lowest COD value but it is not the easiest to be treated, even though LW3 which shows the highest COD is appropriately respected to the lowest removal rate. These facts are confirmed with the percentage of reduced COD suggesting a non-linear correlation correlatedly the COD reduction with the decolorization.

The spectral changes of treated LW1 represents that the absorbance at visible range decreased along with time of treatment [Figure 9a], but there accompanied by the increased absorbance at UV region (250-280 nm) that is associated to the presence of aromatic functional group (Patil et al., 2016) [Figure 9b-9c]. Similar pattern is expressed by the wavelength scan of spectral change for LW2 sample (Figure 9d-9e). The comparison between decolorization and COD reduction and spectral changes of LW1 and LW2 indicate that dyestuffs contaminants were destructed by photocatalytic treatment, but the degradation products are organic or aromatic compounds in detail, so it contributes to a high COD value. The works reported elucidation on the mechanism of photocatalytic degradation of some dyes including methylene blue, rhodamine B, and bromophenol blue exhibited the released aromatics compounds in the photocatalytic-treated solution (Xu et al., 2018; Kuruthukulangara and Asharani, 2024). Conclusively, All LW samples is dominated by the more persistence and colorless compounds rather than dyestuffs.

3.3 Effect of Oxidant and Radical Scavenger

Photocatalytic mechanism over nickel nanoparticles lays on the capability of nanoparticles to produce localized surface plasmon resonance to absorb UV light and induce the photoactivated radicals from the interaction with hydroxyl of water (Talebi et al., 2021). The plausible mechanism is as follows:

$$\begin{aligned} \mathrm{Ni} + h\nu &\rightarrow \mathrm{SPR} \\ 2\mathrm{H}^+ + 2\mathrm{e}^-(\mathrm{SPR}) &\rightarrow \mathrm{H_2} \\ \mathrm{OH}^- + \mathrm{h}^+ &\rightarrow \mathrm{OH}^\bullet \\ \mathrm{e}^-(\mathrm{SPR}) + \mathrm{O_2} &\rightarrow \bullet\mathrm{O_2} \\ \bullet\mathrm{O_2} + (\mathrm{C}_x\mathrm{H}_y\mathrm{O}_z) &\rightarrow \text{Degradation products} \end{aligned}$$

Figure 10 represents the scheme of radical formation and oxidation of organic compounds. The presence of nickel nanoparticles in Biochar/Ni could provide SPR activation by its interaction with photon, and furthermore, the transported electron could be injected into metal oxide into the composite. As identified from EDX analysis that there are Fe, Si, and Al as minor components, the oxide of iron, for example, could accelerate the formation of radicals via the excited electron from valence band into the conductance band.

Referring to the mechanism, the reaction is accelerated by supplying more oxidants to produce reactive oxygen species for oxidizing the organic compounds. Exploration on the effect of oxidant was performed by the addition of H_2O_2 and peroxodisulfate [$S_2O_8^{2-}$] to the decolorization of LW1. The kinetics plots are presented in Figure 11a. Based on the kinetics plots and the pseudo-first order kinetics plot [Figure 11b], it is obtained that the oxidant slightly accelerates the photocatalytic oxidation as indicated by the higher kinetics constant and decolorization efficiency. However, compared to previous works on the utilization of nickel-loaded biochar for methyl violet

Table 4. Evaluated Aspects of Greenness on AGREE Calculation of Photocatalytic, Photocatalytic Oxidation, and MW-Assisted Catalytic Peroxidation of LW

Principle	Photocatalytic treatment	Photocatalytic oxidation treatment	MW-assisted catalytic peroxidation
Principle 1. Direct Analytical Techniques Should Be Applied to Avoid Sample Treatment	in-field sampling and direct analysis	in-field sampling and direct analysis	in-field sampling and direct analysis
Principle 2. Minimal Sample Size and Minimal Number of Samples Are Goals	5 mL	5 mL	5 mL
Principle 3. *In Situ* Measurements Should Be Performed	in line	in line	in line
Principle 4. Integration of Analytical Processes and Operations Saves Energy and Reduces the Use of Reagents	3 or fewer	3 or fewer	3 or fewer
Principle 5. Automated and Miniaturized Methods Should Be Selected	manual, miniaturized	manual, miniaturized	Semi-automatic, miniaturized
Principle 6. Derivatization Should Be Avoided	No problematic compound is identified	No problematic compound is identified	No problematic compound is identified
Principle 7. Generation of a Large Volume of Analytical Waste Should Be Avoided and Proper Management of Analytical Waste Should Be Provided	250 mL	250 mL	250 mL
Principle 8. Multianalyte or Multiparameter Methods Are Preferred versus Methods Using One Analyte at a Time	2 analytes with 25 samples analyzed per hour	2 analytes with 25 samples analyzed per hour	2 analytes with 25 samples analyzed per hour
Principle 9. The Use of Energy Should Be Minimized	UV-Visible spectrophotometry	UV-Visible spectrophotometry	Microwave reactor
Principle 10. Reagents Obtained from Renewable Sources Should Be Preferred	The raw material is biomass-biobased reagent	The raw material is biomass-biobased reagent	The raw material is biomass-biobased reagent
Principle 11. Toxic Reagents Should Be Eliminated or Replaced	No toxic reagent	Use of oxidant	Use of oxidant
Principle 12. The Safety of the Operator Should Be Increased	Persistent and toxic chemicals to aquatic life	Persistent and toxic chemicals to aquatic life	Persistent and toxic chemicals to aquatic life

removal, the elevated values are smaller (Fatimah et al., 2022c). The addition of $S_2O_8^{2-}$ contributed to produce more ROS by the following mechanisms (Lee et al., 2020; Alamgholiloo et al., 2026):

$$Ni + h\nu \rightarrow SPR$$
$$e^-(SPR) + S_2O_8^{2-} \rightarrow \bullet SO_4^- + SO_4^{2-}$$
$$\bullet SO_4^- + H_2O \rightarrow \bullet OH + H^+ + SO_4^{2-}$$
$$\bullet SO_4^-/\ \bullet OH + C_2H_yO_z \rightarrow CO_2 + H_2O + \text{mineralized products}$$

Meanwhile, H_2O_2 forced the oxidation through the following additional mechanism:

$$Ni + h\nu \rightarrow SPR$$
$$e^-(SPR) + H_2O_2 \rightarrow 2\bullet OH$$
$$\bullet OH + O_2 \rightarrow \bullet O_2^- + \bullet OOH$$
$$\bullet O_2^- + C_xH_yO_z \rightarrow \text{degradation products}$$

To explore the underlying photocatalytic oxidation mechanism, the effect of radical scavengers was evaluated. Isopropanol (IPA) and benzoquinone (BQ) were utilized as hydroxyl radical (•OH) and superoxide radical (•OOH), respectively. The effect of scavenger addition on the kinetics of photocatalytic oxidation using $S_2O_8{}^{2-}$ was studied, and the kinetics plots are provided in Figure 11c.

Compared to the photocatalytic oxidation treatment with-

out scavenger which gained decolorization efficiency of 85.21%, the IPA and BQ addition suppressed the decolorization efficiency to 43.50% and 68.38%, respectively [Figure 11d]. These imply that both scavengers act to catch the produced radicals so the propagation and further oxidation to organic compounds are inhibited. By comparing the reduced decolorization efficiency, •OH plays a more important role in the photocatalytic oxidation mechanism rather than •OOH. Photo-generated electrons can activate peroxymonosulfate (PMS), leading to the production of •OH, which furthermore produces $•SO_4^-$ (Fan et al., 2024).

3.4 Microwave-Assisted Catalytic Peroxidation

Intensified catalytic peroxidation is one of the schemes in AOPs with the principle that the collision of activated molecules could be achieved via MW irradiation. The characteristics of MW-irradiated reaction is the less-time consumption as consequence of high acceleration. More efficient energy transfer is achievable by MW irradiation compared to conventional heating as the MW activates the polar ions to vibrate and generate heat towards reaction medium that directly increases the reaction efficiency (Qadariyah et al., 2024). These aspects are applied in catalytic peroxidation. The kinetics plots of MW-assisted catalytic peroxidation towards LW1 samples using varied catalyst dosage are presented in Figure 12a.

In addition, the mass or dosage of catalyst is substantially contributed to the mechanism as the higher decolorization efficiency by 0.2 g/250 mL catalyst compared to that of 0.1 g/250 mL is expressed. However, similar with photocatalytic treatment, the COD reduction is lower compared to decolorization [Figure 12b]. HPLC analysis was employed to elucidate the occurring degradation under MW-assisted procedure. Comparison on the chromatograms revealed that not only does a reduced intensity of the dominant peak at retention time of 1.67 min in LW sample is detected by the treatment for 10 min, but new peak at 0.879 min appeared [Figure 12c]. The peak is directly indicative of degradation product of the catalytic peroxidation.

The high decolorization efficiency (91.29%) is expressed at shorter time of 10 min, and this is higher compared to the efficiency achieved by photocatalysis (78.26%) and photocatalytic oxidation using H_2O_2 (87.22%) in longer time. In the MW-assisted reaction, when catalyst and compounds in the reaction system are irradiated by MW, the radiation causes absorption, projection, and reflection (Puspita et al., 2025). In a medium, these responses will be highly activated to cause friction between the polar molecules and producing a macroscopic thermal effect (Xue et al., 2019; A et al., 2025). In the presence of peroxide, homolytic cleavage is easier to perform, then the oxidation of organic molecules could be faster. Figure 13 describes the interactions during the MW-assisted process.

3.5 Stability of Biochar/Ni

Chemical stability is an important feature required for catalyst and photocatalyst, mainly for applicability in larger industrial scale. Some materials experience changes in surface properties due to the influence of surface oxidation/reduction, surface coverage by target molecules in the reaction and also the release of active catalyst sites during the reaction. To confirm the stability of Biochar/Ni in photocatalysis and also MW-assisted catalytic peroxidation, the used catalyst/photocatalyst was recycled by washing with technical ethanol followed by drying at oven at 60°C prior to further usage until 5th cycle. The stability of Biochar/Ni could be determined by the relative change of decolorization from both procedures. As can be seen from Figure 14, the decolorization reduced along with the recycling and reuse, but the reduced decolorization could be said to be insignificant (less than 10%). These suggest the material could be said to be chemically stable. XRD analysis towards the 5th cycle used material shows a good fitness of the stability, as identified by remained reflections associated to nickel nanoparticles occurrence in the material.

3.6 Greenness Evaluation of the Process

Based on COD analysis of treated solution, it is conclusively obtained that all procedures could not completely remove the organic contaminants in LW samples. The degradation products are persistence chemicals that requires further comprehensive removal procedures. However, as consideration for future development, the greenness of the photocatalytic treatment, photocatalytic oxidation, and MW-assisted catalytic peroxidation of LW using Biochar/Ni was evaluated using the Analytical Greenness Calculator (AGREE)(Pena-Pereira et al., 2020). The assessment was based on the twelve principles of green analytical chemistry including the use of chemicals, analytical method and instrumentation, and sampling amount. Table 4 lists the aspects of each procedure.

By 12 aspects of measurement in AGREE, there are three distinctive aspects among the process. All treatment uses in-field sampling and direct analysis utilizing UV-Visible spectrophotometry with 5 mL of sampling. There are more than 25 samples could be analysed in an hour. For photocatalytic and photocatalytic oxidation treatments, UV-Visible spectrophotometry analysis consumed the higher energy, meanwhile microwave reactor is the most energy consumed instrument, even though the time of treatment is short. Both photocatalytic oxidation and MW-assisted catalytic peroxidation use oxidant either H_2O_2 or $S^2O_8^{2-}$ which potentially toxicant. Specifically, MW-assisted treatment uses semi-automatic and miniaturized procedure and more effective sampling. Based on these measurements, AGREE score and corresponding pie charts are shown in Figure 15.

The overall AGREE score for photocatalytic and MW-assisted catalytic peroxidation treatments are 0.73 and 0.74, respectively, higher than photocatalytic oxidation treatment, 0.71. The higher value reflects the environmentally friendly nature of all stages of the method, including the use of biomass as raw material or bio-based reagent, less consumed energy and semi-automatic process. The combination of high decolorization and COD reduction as treatment performance and

sustainability demonstrates the strong potential of the developed method as an environmentally friendly approach for dye wastewater treatment.

4. CONCLUSIONS

Nickel-loaded biochar (Biochar/Ni) composite derived from orange peel waste has been examined to be photocatalyst and catalyst for laboratory wastewater treatment. Physicochemical characterization of Biochar/Ni using XRD revealed the occurrence of the dispersed nickel nanoparticles with a crystallite size of 34.7 nm. From Raman spectroscopy and VSM analysis, it is concluded that the composite demonstrated regularly graphitic structure and magnetic properties with magnetism of 8.47 emu/g. Towards varied laboratory wastewater, Biochar/Ni exhibited photocatalytic activity for decolorization, even though from the COD analysis, there is incomplete removal of contained contaminants. The decolorization was accelerated by the addition of H_2O_2 and S_2O8_{text} as oxidants in the photocatalytic oxidation system. Moreover, shorter time of decolorization and enhanced COD reduction are expressed by microwave-assisted catalytic peroxidation. Among evaluated processes, the greenness evaluation revealed that microwave-assisted catalytic peroxidation gave the better performance for laboratory wastewater treatment.

5. ACKNOWLEDGEMENT

Authors thank to Direktorat Penelitian dan Pengabdian kepada Masyarakat (DPPM) Universitas Islam Indonesia for Research funding through" Penelitian Unggulan Yayasan Badan Wakaf (SPU YBW)-Akademik" year 2025.

REFERENCES

A, J. K., V. Rippelová, L. McGachy, J. Hendrych, and P. Mašín (2025). Microwave-Enhanced Catalytic Oxidation of VOCs: From Lab-Scale Optimization to Pilot-Scale Industrial Application. *Results in Engineering*, **28**; 108096

Alamgholiloo, H., N. N. Pesyan, S. Badri, and M. Rizehbandi (2026). Developing Ammonium Persulfate Activation by Tri-Metal Oxide-Based Nanocomposite for Upgraded Organic Pollutants Degradation. *Scientific Reports*, **16**; 3109

Bao, T., Q. Wang, Y. Jiang, X. Zhao, and Y. Cao (2024). Multicomponent Nanoparticles Decorating a Lignin-Derived Biochar Composite for 2-Nitrophenol Sensing. *Crystals*, **14**; 506

Barría, Y., A. Burbano, A. James, G. Gascó, and A. Méndez (2025). Sorption Capacity of Biochars Obtained by Gasification of Rice Husks and Wild Sugarcane: Removal of Malachite Green and Arsenic from Water Solutions. *Biomass Conversion and Biorefinery*, **15**(2); 2131–2143

Bekru, A. G., L. T. Tufa, O. A. Zelekew, M. Goddati, J. Lee, and F. K. Sabir (2022). Green Synthesis of a CuO−ZnO Nanocomposite for Efficient Photodegradation of Methylene Blue and Reduction of 4-Nitrophenol. *ACS Omega*, **7**; 30908–30919

Bhakta, A. K., L. Znaidi, E. Blanc, N. Challab, P. Decorse, A. Vega, D. Vrel, S. Ammar, and S. Prasanna (2025). Maple Wood Biochar-Supported Nickel Nanoparticles: One-Pot Synthesis for Simultaneous Removal of Cationic and Anionic Dye Mixture. *Next Sustainability*, **6**; 4–11

El-Nemr, M. A., M. Yılmaz, S. Ragab, and A. El Nemr (2024). Biochar-SO Prepared from Pea Peels by Dehydration with Sulfuric Acid Improves the Adsorption of Cr^{6+} from Water. *Biomass Conversion and Biorefinery*, **14**(2); 2601–2619

Eltaweil, A. S., A. M. Abdelfatah, M. Hosny, and M. Fawzy (2022). Novel Biogenic Synthesis of a Ag@ Biochar Nanocomposite As an Antimicrobial Agent and Photocatalyst for Methylene Blue Degradation. *ACS omega*, **7**(9); 8046–8059

Fan, X., Q. Fu, G. Liu, H. Jia, X. Dong, and Y. Li (2024). Applying Molecular Oxygen for Organic Pollutant Degradation: Strategies, Mechanisms, and Perspectives. *Environmental Science and Ecotechnology*, **22**; 100469

Fatimah, I., G. Fadillah, I. Yanti, and R.-a. Doong (2022a). Clay-Supported Metal Oxide Nanoparticles in Catalytic Advanced Oxidation Processes: A Review. *Nanomaterials*, **12**(5); 825

Fatimah, I., G. Purwiandono, I. Sahroni, A. Wijayana, M. Faraswati, A. D. Putri, W.-C. Oh, and R.-a. Doong (2022b). Magnetically-Separable Photocatalyst of Magnetic Biochar from Snake Fruit Peel for Rhodamine B Photooxidation. *Environmental Nanotechnology, Monitoring & Management*, **17**; 100669

Fatimah, I., G. D. Ramanda, S. Sagadevan, Suratno, M. Tamyiz, and R. Doong (2024). One-Pot Synthesis of Nickel Nanoparticles-Embedded Biochar and Insight on Adsorption, Catalytic Oxidation, and Photocatalytic Oxidation of Dye. *Case Studies in Chemical and Environmental Engineering*, **10**; 100767

Fatimah, I., H. K. Wijayanti, G. D. Ramanda, M. Tamyiz, R. Doong, and S. Sagadevan (2022c). Nanocomposite of Nickel Nanoparticles-Impregnated Biochar from Palm Leaves as Highly Active and Magnetic Photocatalyst for Methyl Violet Photocatalytic Oxidation. *Molecules*, **27**; 6871

Fitri, E. S., R. Mohadi, N. R. Palapa, S. A. Rachman, and A. Lesbani (2024). Selective Removal of Anionic and Cationic Dyes Using Magnetic Composites. *Science and Technology Indonesia*, **9**(1); 129–136

Fouda, S. H., E. S. A. El-Halim, and H. A. A. Ghany (2025). Radiological and Chemical Hazards of Persistent Organic Pollutants in the Textile Sector. *Scientific Reports*, **15**; 3581

Hu, W., X. Zhang, M. Chen, S. T. Rahman, X. Li, and G. Wang (2024). Enhancing Cr(VI) Adsorption of Chestnut Shell Biochar through H_3PO_4 Activation and Nickel Doping. *Molecules*, **29**; 1022

Hunter, R. D. and J. Ram (2022). Iron-Catalyzed Graphitization for the Synthesis of Nanostructured Graphitic Carbons. *Journal of Materials Chemistry A*, **10**; 4489–4516

Jahani, F., B. Maleki, M. Mansouri, Z. Noorimotlagh, and S. A. Mirzaee (2023). Enhanced Photocatalytic Performance

of Milkvetch-Derived Biochar Via Zno–Ce Nanoparticle Decoration for Reactive Blue 19 Dye Removal. *Scientific Reports*, **13**(1); 17824

Khan, M. N., M. Siddique, N. Mirza, R. Khan, M. H. Abdellattif, G. E. Batiha, A. Al-Harrasi, and A. Khan (2022). Synthesis, Characterization, and Application of Ag-Biochar Composite for Sono-Adsorption of Phenol. *Frontiers in Environmental Science*, **10**(1); 823656

Kuruthukulangara, N. and I. V. Asharani (2024). Photocatalytic Degradation of Rhodamine B, a Carcinogenic Pollutant, by MgO Nanoparticles. *Inorganic Chemistry Communications*, **160**(1); 111873

Lee, J., U. Von Gunten, and J.-H. Kim (2020). Persulfate-Based Advanced Oxidation: Critical Assessment of Opportunities and Roadblocks. *Environmental Science & Technology*, **54**(6); 3064–3081

Lesbani, A., P. Mega, S. Bahar, N. Siregar, N. R. Palapa, T. Taher, and F. Riyanti (2021a). Adsorptive Removal of Methylene Blue Using Zn/Al LDH Modified Rice Husk Biochar. *Polish Journal of Environmental Studies*, **30**(4); 3117–3124

Lesbani, A., N. R. Palapa, R. J. Sayeri, T. Taher, and N. Hidayati (2021b). High Reusability of NiAl LDH/Biochar Composite in the Removal of Methylene Blue from Aqueous Solution. *Indonesian Journal of Chemistry*, **21**(2); 421–434

Li, J., T. Liu, and Z. Wang (2024). One-Pot Synthesis of Biochar from Industrial Alkali Lignin with Superior Pb(II) Immobilization Capacity. *Molecules*, **29**(18); 4310

Li, S., Y. Wu, H. Zheng, H. Li, Y. Zheng, J. Nan, J. Ma, D. Nagarajan, and J.-S. Chang (2023). Antibiotics Degradation by Advanced Oxidation Processes (AOPs): Recent Advances in Ecotoxicity and Antibiotic-Resistance Genes Induction of Degradation Products. *Chemosphere*, **311**(1); 136977

Methneni, N., J. A. Morales-González, A. Jaziri, H. B. Mansour, and M. Fernandez-Serrano (2021). Persistent Organic and Inorganic Pollutants in the Effluents from the Textile Dyeing Industries: Ecotoxicology Appraisal Via a Battery of Biotests. *Environmental Research*, **196**; 110956

Moavi, J., F. Buazar, and M. H. Sayahi (2021). Algal Magnetic Nickel Oxide Nanocatalyst in Accelerated Synthesis of Pyridopyrimidine Derivatives. *Scientific reports*, **11**(1); 6296

Moradi, P. and M. Hajjami (2022). Stabilization of Ruthenium on Biochar-Nickel Magnetic Nanoparticles as a Heterogeneous, Practical, Selective, and Reusable Nanocatalyst for the Suzuki C–C Coupling Reaction in Water. *RSC Advances*, **12**(21); 13523–13534

Moreno, R., A. Pinheiro, G. Sim, M. Thyrel, J. J. Alcaraz-Espinoza, S. H. Larsson, and H. P. de Oliveira (2022). Facile Synthesis of Sustainable Biomass-Derived Porous Biochars as Promising Electrode Materials for High-Performance Supercapacitor Applications. *Nanomaterials*, **12**(5); 866

Palapa, N. R., Z. A. Zahara, R. Mohadi, I. Royani, and A. Lesbani (2024). High Performance of Ni−Al/Magnetite Biochar for Methyl Orange Removal in Aqueous Solution. *Science and Technology Indonesia*, **9**(2); 156–166

Patil, N. P., J. Shaikh, B. P. Kapadnis, and V. B. Gaikwad (2016). Decolourisation of Dyes and Their Mixture by *Providencia* sp. VNB7 Isolated from Textile Effluent Treatment Plant. *Journal of Industrial Pollution Control*, **32**(2); 623–628

Pena-Pereira, F., W. Wojnowski, and M. Tobiszewski (2020). AGREE-Analytical Greenness Metric Approach and Software. *Analytical Chemistry*, **92**(14); 10076–10082

Phyu, P., L. Chandana, V. V. S. S. Srikanth, G. Madras, and S. Ch (2023). Biowaste-Derived Ni/NiO-Decorated 2D Biochar for Adsorption of Methyl Orange. *Journal of Environmental Management*, **344**(1); 118418

Puspita, O. E., M. I. Sulistyowaty, R. Salam, and D. Setyawan (2025). Microwave-Assisted Synthesis: A Green Chemistry Approach for Drug Cocrystals. *Science and Technology Indonesia*, **10**(4); 1130–1147

Qadariyah, L., D. S. Ryvalda, N. Y. Aditama, V. Aswie, and M. Mahfud (2024). Methyl Ester Sulfonate (MES) Surfactant Production from Waste Cooking Oil (WCO) with Microwave Technology. *Science and Technology Indonesia*, **9**(4); 929–940

Rahayu, N., N. Juleanti, R. Mohadi, T. Taher, and A. Rachmat (2020). Copper Aluminum Layered Double Hydroxide Modified by Biochar and Its Application as an Adsorbent for Procion Red. *Journal of Water and Environment Technology*, **18**(5); 359–371

Rehman, Z. U., M. Nawaz, H. Ullah, I. Uddin, S. Shad, E. Eldin, R. A. Alshgari, A. Ahmed, A. Bahajjaj, W. U. Arifeen, and M. S. Javed (2023). Synthesis and Characterization of Nickel Nanoparticles via the Microemulsion Technique and Its Applications for Energy Storage Devices. *Materials*, **16**(1); 325

Talebi, P., H. Singh, E. Rani, M. Huttula, and W. Cao (2021). Surface Plasmon-Driven Photocatalytic Activity of Ni@NiO/$NiCO_3$ Core–Shell Nanostructures. *RSC Advances*, **11**(5); 2733–2743

Thiruvenkatachari, R., S. Vigneswaran, and I. S. Moon (2008). A Review on Uv/TiO_2 Photocatalytic Oxidation Process (Journal Review). *Korean Journal of Chemical Engineering*, **25**(1); 64–72

Tomczyk, A., Z. Sokołowska, and P. Boguta (2020). Biochar Physicochemical Properties: Pyrolysis Temperature and Feedstock Kind Effects. *Reviews in Environmental Science and Biotechnology*, **19**(2); 191–215

Vilas-Boas, A. A., D. Magalhães, R. Gómez-García, D. A. Campos, and M. Correia (2025). Upcycled Orange Peel Ingredients: A Scoping Review on Phytochemical Composition, Extraction Techniques, and Biorefinery Strategies. *Foods*, **14**(21); 3766

Wanapat, M., C. Suriyapha, G. Dagaew, R. Prachumchai, S. Phupaboon, S. Sommai, and M. Matra (2024). The Recycling of Tropical Fruit Peel Waste-Products Applied in Feed Additive for Ruminants: Food Manufacturing Industries, Phytonutrient Properties, Mechanisms, and Future Applications. *Journal of Agriculture and Food Research*, **17**(1); 101234

Xu, D., X. Song, W. Qi, H. Wang, and Z. Bian (2018). Degradation Mechanism, Kinetics, and Toxicity Investigation of 4-Bromophenol by Electrochemical Reduction and Oxidation with Pd−Fe/Graphene Catalytic Cathodes. *Chemical Engineering Journal*, **333**(1); 477–485

Xue, C., Y. Mao, W. Wang, Z. Song, X. Zhao, J. Sun, and Y. Wang (2019). Current Status of Applying Microwave-Associated Catalysis for the Degradation of Organics in Aqueous Phase: A Review. *Journal of Environmental Sciences*, **81**(1); 119–135

Yan, Y., S. Manickam, E. Lester, T. Wu, and C. Heng (2021). Synthesis of Graphene Oxide and Graphene Quantum Dots from *Miscanthus* via Ultrasound-Assisted Mechano-Chemical Cracking Method. *Ultrasonics Sonochemistry*, **73**(1); 105519

Yeboah, M. L., X. Li, and S. Zhou (2020). Facile Fabrication of Biochar from Palm Kernel Shell Waste and Its Novel Application to Magnesium-Based Materials for Hydrogen Storage. *Materials*, **13**(3); 625

Zulqarnain, S. Kim, D. Chun, J. Yoo, S. J. Yoon, S.-J. Kim, and S.-J. Park (2025). Low-Temperature Steam Reforming of Toluene as a Biomass Tar Model Compound Over Biochar-Supported Catalysts. *Biochar*, **7**(1); 42

